Development of an Adiabatic RF Neutron Spin Flipper at the China Spallation Neutron Source[*]

Xu Qin,[1,2] Yu-Chen Dong,[3,2,4,5] Wolfgang Kreuzpaintner,[3,2,4] Xiao-Mian Li,[6] Xin-Pei Meng,[6] Matthew Musgrave,[3,2,4] Xiao-Min Xiong,[1] Fan Ye,[3,2,4] Jun-Pei Zhang,[3,2,4] Tian-Hao Wang,[3,2,4,†] and Xin Tong[3,2,4,‡]

[1]*Center for Neutron Science and Technology, Guangdong Provincial Key Laboratory of Magnetoelectric Physics and Devices, School of Physics, Sun Yat-Sen University, Guangzhou, Guangdong 510275, China*
[2]*Spallation Neutron Source Science Center, Dongguan 523803, China*
[3]*Institute of High Energy Physics, Chinese Academy of Sciences, Beijing 100049, China*
[4]*Guangdong Provincial Key Laboratory of Extreme Conditions, Dongguan, 523803, China*
[5]*School of Nuclear Science and Technology, University of Chinese Academy of Sciences, Beijing 100049, China*
[6]*Mechatronics Technology R&D and Service Center, Dongguan Polytechnic, Dongguan 523808, China*

A new prototype adiabatic RF-flipper was recently developed at the China Spallation Neutron Source. The prototype device was calibrated at the test beamline BL-20 over a wavelength range of 0.6 Å to 5.5 Å, and achieved a flipping efficiency of 97% for neutron wavelengths above 4 Å. During the development of the adiabatic RF-flipper, finite element method and spin transformation simulations were applied to precisely determine the magnetic field configuration and neutron spin-flip efficiency. This work demonstrates the design and optimization of the adiabatic RF-flipper for a specific neutron beamline, where the dependence of the flipping efficiency on neutron wavelength can be analyzed through simulation and numerical calculation for pulsed neutron beams.

Keywords: neutron spin-flipper, polarized neutron, spallation neutron source

I.   INTRODUCTION

Neutron scattering is a widely used method for physics and material research. In recent years, several large-scale neutron facilities have been developed across the world to advance neutron scattering techniques and applications. Existing neutron facilities have also undergone continuous upgrades to allow for many cutting-edge scientific measurements. Among neutron scattering experimental methods, polarized neutrons play a key role and have a wide range of applications. This is especially true for weak magnetic scattering, where advanced neutron polarization instruments are usually required for effective measurements [1]. Instruments that can utilize polarized neutrons include Small-Angle Neutron Scattering (SANS), neutron reflectometry, neutron imaging, neutron diffraction, inelastic neutron scattering and Neutron Spin-Echo (NSE) [2–12].

With the support of polarized neutron techniques, many new experimental methods have emerged that contribute to research in various fields [13–20]. Notable techniques include longitudinal polarization analysis, XYZ polarization analysis, and Spherical Neutron Polarimetry (SNP). Longitudinal polarization analysis involves performing neutron spin analysis along a one-dimensional direction in experiments, allowing for the measurement and analysis of non-spin-flip and spin-flip cross-sections under specific scattering geometries, where the applied magnetic field (guide field) is often applied to adjust the polarization of the incident neutron beam, providing magnetic information about the materials. XYZ polarization analysis is suitable for simultaneous measurements in a multidetector polarization analysis experiment, but it still poses difficulties in measuring the spin rotation quantities related to chiral magnetic scattering. The SNP establishes a zero magnetic field region to shield the magnetic field, enabling precise general polarization analysis over a wide scattering angle range. For all mentioned techniques, controlling the neutron spin state during the measurement is an essential step. The neutron spin flipper (NSF) is widely used in polarized neutron experiments due to its capability to control the neutron spin state [21–23]. In modern neutron experiments, using a spin flipper with high transmission and excellent flipping efficiency is crucial because it can improve the experiment's precision and simplify the measurement procedure and data analysis.

Over the past decades, various types of spin flippers were developed to satisfy the demands of different neutron sources. These include Mezei flippers [10], Drabkin spin flippers [24], thin film flippers [25], resonant RF-flippers [26], superconductor-based flippers [16, 27–29], and adiabatic RF-flippers [30, 31]. Due to their nature of controlled precession, the Mezei flipper and thin film flippers are limited to one specific neutron wavelength at a time. Whereas an adiabatic RF-flipper can simultaneously support a wide range of neutron wavelengths and allow neutron beams with larger fluxes to pass through without any neutron scattering or absorbing. It is used as a key piece of equipment in high-resolution material dynamics studies in NSE, reducing background signals in neutron scattering experiments, and in other experimental techniques using wide wavelength spectrum po-
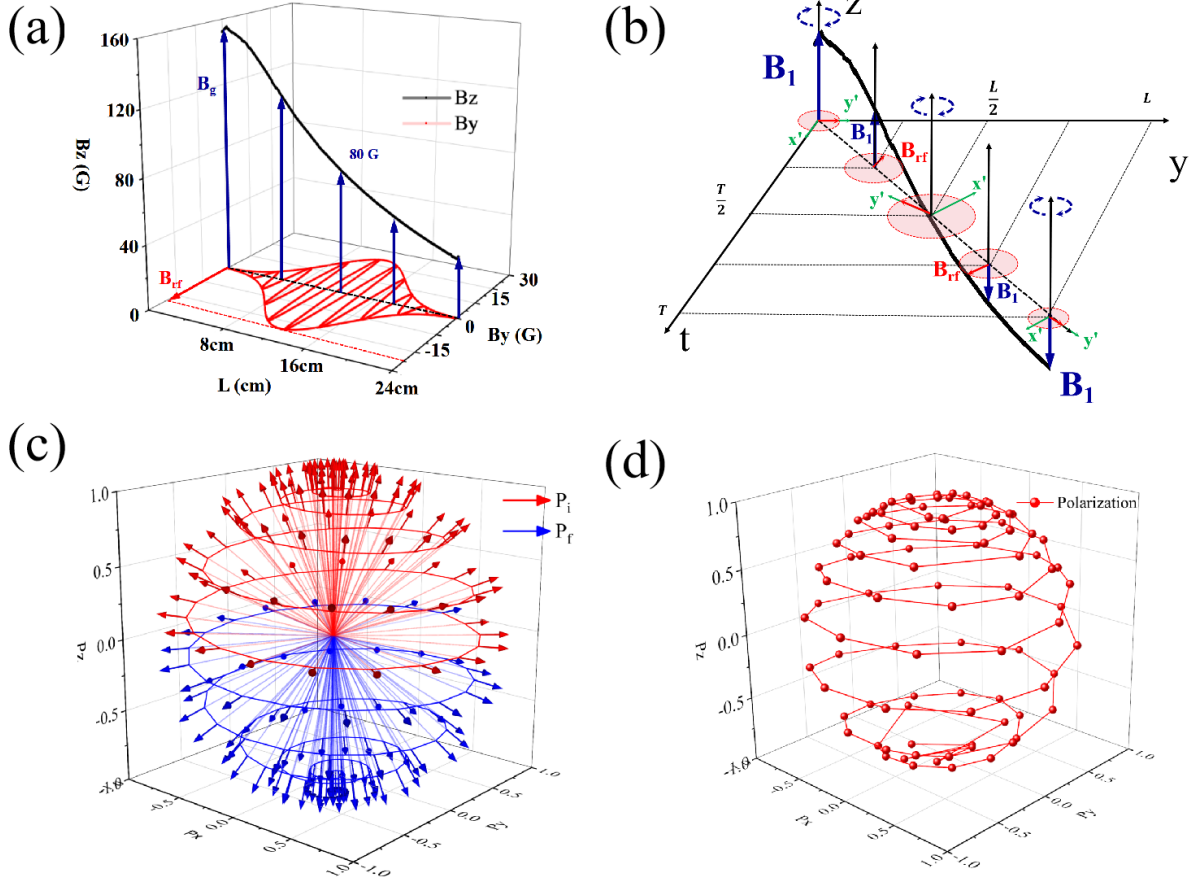
Fig. 1. (a) The laboratory frame is applied in this design. The direction of the neutron beam and the RF-field ($\mathbf{B}_{RF}$) are parallel to the y-axis, and the gradient field ($\mathbf{B}_1 = \mathbf{B}_g - \mathbf{B}_0$) direction is set as the z-axis. l is the length of the flipper. (b) The rotating frame rotates uniformly clockwise along the z-axis with an angular velocity ω. In the rotating frame, the RF-field component (rotating with the frame) is parallel to the y'-axis, the gradient field $\mathbf{B}_g$ is parallel to the z-axis, and the RF-field component rotating at a different frequency is neglected. (c-d) The orientation of the neutron polarization in the adiabatic RF-flipping process. (c) Theoretical progression of a 4 Å neutron polarization vector within an ideal linear field (from 130 to 70 G). (d) Calculated progression of a 4 Å neutron polarization vector for the designed adiabatic RF-flipper fields $\mathbf{B}_g$ and $\mathbf{B}_{RF}$ shown in Fig. 1.

larized neutrons. With the development of modern neutron sources, time-of-flight based neutron instruments at pulsed neutron sources require more detailed design, such as Spallation Neutron Source (SNS) at Oak Ridge National Laboratory (ORNL), Material and Life Science Experimental Facility at Japan Proton accelerator Research Complex (J-Parc) and the China Spallation Neutron Source (CSNS). Especially for newly developed beamlines, it is advantageous to consider polarization capability during the design and construction process, so that optics and magnetic field configurations can be collectively optimized.

For a typical time-of-flight neutron beamline, the combination of a polarizing supermirror and an adiabatic RF-flipper is one of the few solutions to generate polarization and control the spin state for a wide-range of neutron wavelengths with high polarization and transmission efficiency. The polarizing supermirror and flipper combination usually serves as a sub-stitutional part of the neutron guide, and hence contribute to the overall neutron beam optics. Two options exist for deploying the polarizing supermirror and adiabatic RF-flipper.

One option is to place the two components at the beginning of the neutron guide section where the neutron beam has lower cross-sectional area and divergence, so that undesired reflections from the supermirror can be avoided. For such a configuration, the neutron polarization must be transferred to the sample position by a relatively long guide field system, and the adiabatic RF-flipper must be incorporated with the neutron guide across. Typical beamlines such as the GP-SANS at ORNL, LET cold neutron multi-chopper spectrometer, and Larmor SANS/SESANS beamline at the ISIS neutron and Muon Source (UK) adopt such a design during commissioning. The other option is to install the polarizing supermirror and adiabatic RF-flipper within close approximate to the sample, usually inside the scattering room for easy access

and experiment flexibility. However, such configurations usually require more sophisticated control of the magnetic field design because the sample stage and magnetic field environment affect the performance of the adiabatic RF-flipper and polarization transfer. In general, this configuration is less restrictive on the neutron beam optics but would still require the adiabatic RF-flipper to be compatible with neutron flight tubes for better transmission.

In this study, we detail the development of the first in-house manufactured adiabatic RF-flipper at the CSNS which provides a platform for conducting scientific research in many frontier disciplines [32–34]. The prototype device is tested with a time-of-flight polarized neutron beam for performance calibration. The optimization process of the device's key parameters is also explained, along with a comparison between the simulated results and experiment data. The results show that with numerical simulations precise control of the neutron polarization can be predicted, thereby facilitating customization of future adiabatic RF-flippers at the CSNS for different polarized neutron experiments.

II. PRINCIPLES OF RF-FLIPPING

The principles of spin flipping by adiabatic fast passage (AFP) are well established [35], accomplishing spin flips through a helical spinning process achieved by a combination of gradient fields and a corresponding radio-frequency field (RF-field). The two fields are set perpendicular to each other along the neutron path, as shown in Fig. 1(a), with the direction of the gradient field $\mathbf{B}_g$ inside the flipper along the z direction in the laboratory frame. The RF-field ($\mathbf{B}_{\mathrm{RF}}$) is parallel to the neutron flight path and along the y-direction. The magnitudes of both fields are plotted with respect to the distance (l) from the entrance into the RF-flipper region, illustrating their spatial variations.

The gradient field $\mathbf{B}_g$ can be decomposed into two components $\mathbf{B}_0 + \mathbf{B}_1$, with $\mathbf{B}_0$ as the constant "center field" that defines the frequency of $\mathbf{B}_{\mathrm{RF}}$ as $\omega_{\mathrm{RF}} = -\gamma_n \mathbf{B}_0$, where γ_n is the neutron gyromagnetic ratio. The varying component $\mathbf{B}_1$ decreases from positive to negative along the neutron flight path. The RF-field $\mathbf{B}_{\mathrm{RF}}$ is generated by a solenoid with the defined frequency ω_{RF}, and its maximum magnitude aligns at the center position where $\mathbf{B}_g = \mathbf{B}_0$, so that the adiabatic RF-flipping condition is achieved.

In the adiabatic RF-flipping condition, the neutron polarization undergoes a flipping process, which is commonly described in a rotating frame about the z-axis with a frequency of ω_{RF} as shown in Fig. 1(b). Within the rotating frame, polarization along the z-axis is consistent with the laboratory frame, while the effective magnetic field along the z-axis $\mathbf{B}_g$ is reduced by $\mathbf{B}_0$ so that only $\mathbf{B}_1$ remains. In the rotating frame, the RF-field component ($\frac{1}{2}B_{\mathrm{RF}}(l)$) rotating with the frame is parallel to the y'-axis, the gradient field $\mathbf{B}_1$ is parallel to the z-axis, and the RF-field component rotating at $\omega = -2\omega_{\mathrm{RF}}$ is neglected. The RF-field $\mathbf{B}_{\mathrm{RF}}$ is decomposed into a $\frac{1}{2}|B_{\mathrm{RF}}(l)|$ component parallel to the y'-axis and a fast counter-rotating component that is usually neglected. The effective magnetic field $\mathbf{B}_e$ experienced by the neutron is then transformed as follows:

$$\mathbf{B}_e = B_1(l)\hat{\mathbf{z}}' + \frac{1}{2}B_{\mathrm{RF}}(l)\hat{\mathbf{y}}' \qquad (1)$$

The neutron polarization undergoes an adiabatic change from $+\hat{\mathbf{z}}'$ into $+\hat{\mathbf{y}}'$ and then $-\hat{\mathbf{z}}'$ within the rotating frame, as long as the adiabatic condition in Eq. (2) is satisfied:

$$\left| \frac{d}{dt}\left(B_1(l) + \frac{1}{2}B_{\mathrm{RF}}(l) \right) \right| \ll 2\pi\gamma_n \left| B_1(l) + \frac{1}{2}B_{\mathrm{RF}}(l) \right|^2 \qquad (2)$$

The adiabatic transition in the rotating frame becomes a helical trajectory when transformed back to the laboratory frame, as shown in Fig. 1(c). The initial polarization vector $\mathbf{P}_i$ moves towards the xy-plane along red helical lines, and then aligns with the z-axis in the opposite direction as shown by the blue helical lines. The final polarization vector $\mathbf{P}_f$ is antiparallel to the z-axis.

The initial step in designing the prototype adiabatic RF-flipper involved tailoring the gradient magnetic field to the anticipated magnetic field environment. The magnetic field in the RF-flipper is presented in Fig. 1(a), and the calculated evolution of the polarization vector is depicted in Fig. 1(d). To assess the RF-flipping process, the magnetic field is transformed into a rotating frame, as illustrated in Fig. 1(b), and the adiabaticity of the spin flip transformation in the rotating frame is examined using Eq. (2). This process is repeated for multiple iterations of the magnetic field design, and the optimized design is fabricated into a prototype for characterization tests and neutron experiments. Further analysis of the neutron polarization progression is conducted with measurements of the prototype's magnetic field, and this is compared to the neutron flipping efficiency measured with a neutron beamline. This comparison provides insights into the flipping performance and design accuracy across a range of neutron wavelengths, which will guide future optimization. Additionally, the research demonstrated the resilience of the prototype device to external magnetic field influences, which is discussed further in the manuscript.

III. MAIN COMPONENTS DESIGN

The RF-flipper prototype is designed based on the principles previously discussed and consists of six main components, shown in Fig. 2, where 1. Enclosure of the device. 2. Iron plates and permanent magnets generating gradient magnetic field. 3. Detection coil. 4. Solenoid generating the RF-field. 5. Front and 6. Back guide fields composed of iron plates and permanent magnets. The enclosure of the RF-flipper is composed of several non-magnetic bakelite pieces, which ensure the stability of the magnetic field inside the flipper. The gradient field in the z-direction is generated by symmetrically installed iron plates and permanent magnets. The central iron plates are tilted by ± 25-degrees from the horizontal plane. The iron plates have dimensions of $28\,\mathrm{cm} \times 10\,\mathrm{cm} \times 0.2\,\mathrm{cm}$. Six $\mathrm{Nd_2Fe_{14}B}$ magnets
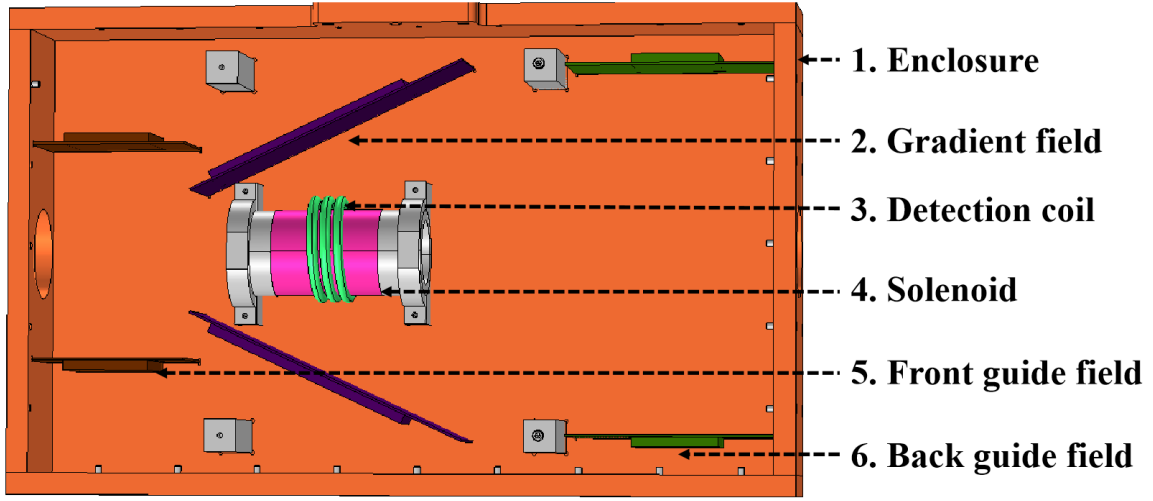
Fig. 2. Cross-sectional schematic view of the adiabatic RF-flipper prototype.

(4 cm × 2 cm × 1 cm) are attached to the iron plates to generate a gradient field ranging from 160 G to 40 G along the neutron flight path. This gradient field is nonlinear, and the center field $B_0 = 80$ G is generated near the geometrical center of the iron plates. Guide fields are installed both upstream and downstream of the central magnetic field components to isolate external stray magnetic fields. Each guide field component consists of a pair of iron plates with dimensions of 15 cm × 8 cm × 0.2 cm.

The solenoid is a single-layer coil 10.25 cm long and 8 cm in diameter with 93 turns of 1.1 mm enamel-coated copper wire wound onto a plastic-steel (Polyvinyl Chloride) substrate. The inductance of the coil should ideally be 0.54 mH and is measured at 0.40 mH with an RLC digital bridge. The solenoid is fixed between two tilted iron plates, generating the RF-field $\mathbf{B}_{RF}$. The solenoid creates an effective RF field region approximately 24 cm long between the gradient field generating iron plates and can accommodate a 6 cm diameter neutron beam passing through the spin flipper. The detection coil consists of three rounds of wire wrapped around the solenoid, which can be moved along the solenoid to monitor the generated RF-field at different locations. The solenoid is powered by a sine-wave current generated from a standard function generator and amplified by a 70 W RF-amplifier.

A matching circuit (match-box) tunes the RLC circuit of the solenoid to ensure sufficient RF-power can be forwarded into the solenoid. The components of the matching box include a protective casing, a cooling fan, and resistive and capacitive components of the RLC circuit. The external solenoid of the RF-flipper creates the inductance of the RLC circuit. The resonant frequency (f) of the RLC circuit is set to be consistent with the neutron Larmor precession frequency defined by B_0 and consequently leads to a capacitance of 1150 pF for the match-box.

Due to the influence of thermal perturbations and wire-contact resistance/capacitance, the resonant frequency of the RLC-circuit may shift and result in a reduced power output at the set frequency of ω_{RF}. The solenoid circuit is designed to generate sufficient magnetic field at ω_{RF} frequency when its total output is above $1/\sqrt{2}$ times the maximum power, thus allowing for a flexible "bandwidth" of the RLC-circuit resonance frequency. This is achieved by introducing a proper resistance load into the match-box circuit. The resistors affect the quality factor (Q) of the RLC circuit, and the dependence between Q and R, as well as the corresponding bandwidth, is shown in Fig. 3(b).

The RLC circuit bandwidth and output power are optimized for the design with a $10.00\,\Omega$ resistor and a $2.05\,\Omega$ solenoid, resulting in a bandwidth of 4.79 kHz and a quality factor of 48.94. Fig. 3(a) illustrates the RLC circuit diagram for the developed system, where V represents the power source composed of a standard function generator and RF-amplifier, R is the total resistance of the circuit, C is the total capacitance, and L is the inductance of the solenoid. Using multiple resistors and capacitors in an RLC circuit can increase the heat dissipation area and improve the thermal stability of the circuit.

The RLC circuit is then tested with a total power up to 70 W, and the result is shown in Fig. 3(c-e). In Fig. 3(c), when the RF-power of the sine-wave signal is input into the RLC circuit, a stable sine-signal can be detected by the detection coil using Faraday's electromagnetic induction law, which indicates that the designed RLC circuit generates an RF-field with the same waveform and frequency as the source signal.

The strength of the RF-field monitored by the detection coil peaks around 234.70 kHz with a bandwidth of 4.82 kHz (from 232.26 kHz to 237.08 kHz), as shown in Fig. 3(d). The tested RLC resonance frequency is 1.44 kHz above the design frequency $\omega_{RF} = 233.26$ kHz, and the bandwidth exceeds the design value by 0.03 kHz. These minor discrepancies are caused by the BNC cable and solenoid connecting wire not being included in the design process. However, the resulting prototype functions sufficiently well to cover the neutron RF-flipping conditions.
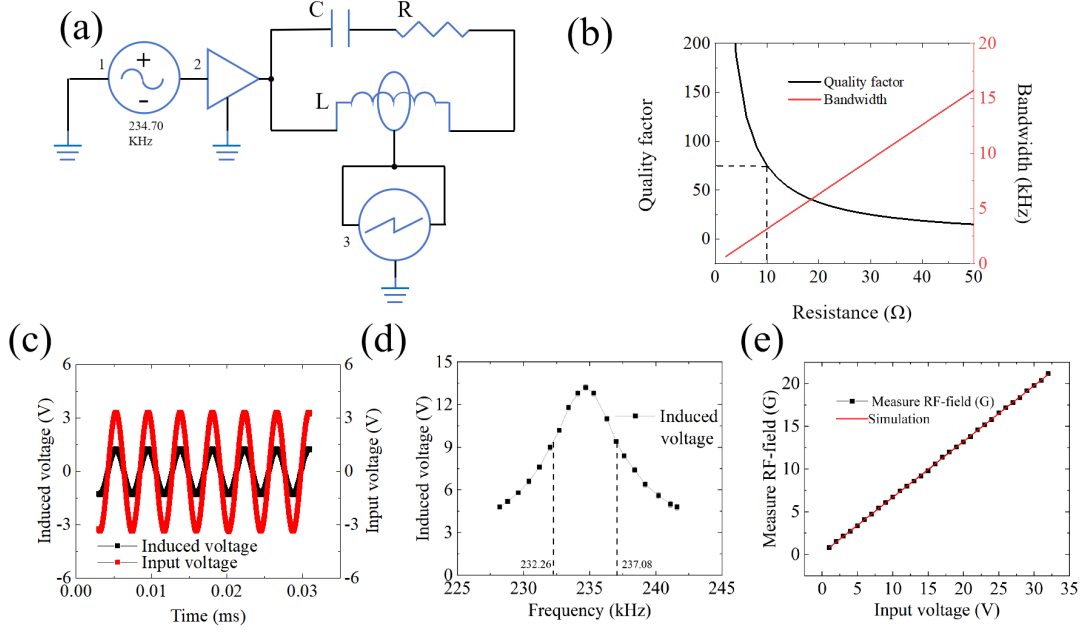
Fig. 3. (a) Schematic diagram of the RLC circuit and detection circuit. 1, 2, and 3 are respectively the function generator, RF-amplifier, and oscilloscope. (b) The resistance dependence of Q (black line, left axis) and bandwidth (red line right axis). (c) The red line is the waveform signal generated from the function generator, and the black line is the induced signal from the detection coil. (d) The frequency dependence of the RF-field measured by the induced signal in the detection coil. (e) The input voltage dependence of the RF-field measured with the detection coil.

Fig. 3(e) shows the induced magnetic field strength measured by the detection coil as the input voltage increases. The slope obtained after performing a linear fit on the dependency between the RF field and the input voltage is 0.65, indicating that the input power of the solenoid is stable and not significantly affected by voltage fluctuations. By combining the magnetic field formula of the energized solenoid with Faraday's law of electromagnetic induction, the slope can be calculated based on the parameters of the solenoid and detection coil. The magnetic field inside the solenoid is generated by the input voltage and can be approximated with $B = \mu_0 \frac{NI}{L_0}$, where μ_0 is the permeability of air, N is the number of turns in the solenoid, L_0 is the length of the solenoid, and I is the current flowing through the solenoid. The relationship between the RF-field and the induced electromotive force is $E = -n\frac{d\Phi}{dt}$, where E is the induced electromotive force in the detection coil, n is the number of turns in the detection coil, and Φ is the magnetic flux on the cross-section of the detection coil. The calculated ratio between the measured RF magnetic field and input voltage is 0.71, while the fitted slope obtained from measurements is 0.65. There are three main reasons for this deviation. Firstly, the solenoid has a finite length, resulting in a center magnetic field that is only approximated equal to that of an infinite solenoid. Secondly, the detection coil is wound around the center of the solenoid, which makes it susceptible due to measurement position. Thirdly, as the operating time increases, variations in resistance and ca-

pacitance parameters may lead to a slight decrease in the RF field generated by the circuit.

IV. SIMULATIONS OF MAGNETIC FIELDS AND NEUTRON POLARIZATION

The gradient fields generated by the main components are simulated using the three-dimensional finite element method in COMSOL Multiphysics® software to establish a magnetic field model of the device [36]. In the simulated model, the relative permeability of the iron plate is 6400, which is calculated based on the hysteresis loop of the actual iron plate. The material of the permanent magnet is N35, and its residual magnetic flux density modulus reaches as high as 1.2T. Using the magnetic field interface in the AC/DC module, the induced magnetic field generated by the permanent magnets is calculated at different angles based on Ampere's Law. In the region of the solenoid where polarized neutrons pass through, the *extremely fine mesh* that is the default setting in COMSOL is adopted, while in other regions, the larger *extra fine mesh* is used. This method of mesh division aims to ensure computational efficiency while maintaining sufficient mesh density to improve simulation accuracy. The design feature of adding a guiding field inside the flipper aims to reduce external magnetic interference and enhance its stability. Therefore, this model does not include the guiding magnetic fields outside
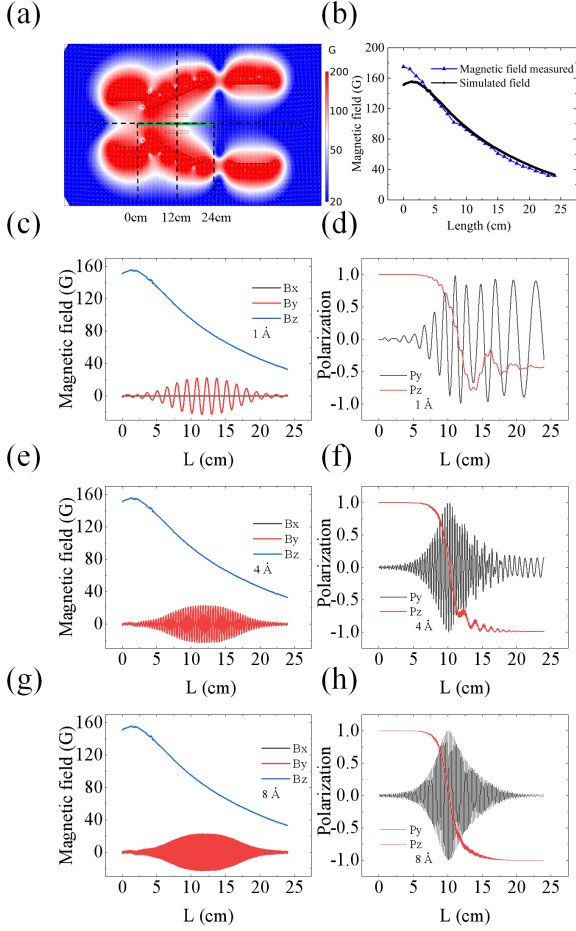
Fig. 4. (a) Cross-sectional view of the flux distribution in the neutron path. The white arrows are the directions of the magnetic field lines. The horizontal green line is the center line of the RF-field region generated by the 10 cm long solenoid. (b) The black line represents the one-dimensional vertical magnetic field distribution at the specific position indicated by the green line in (a). The magnetic field traversed by neutrons of (c) 1 Å, (e) 4 Å, and (g) 8 Å in the laboratory frame. The blue line represents the actual one-dimensional vertical magnetic field distribution measured along the center axis of the solenoid, with the starting point of L at 0 cm in (a). The red line represents the RF-field experienced by neutrons of different wavelengths in (c), (e) and (g). The RF-field has a position dependent profile with a maximum value of 22 G at the center of the solenoid, corresponding to the measured RF-field at the maximum input power in Fig. 3(e). The gradient magnetic field (blue line) is the simulated field from (b). The neutron polarization calculated for neutron wavelengths of (d) 1 Å, (f) 4 Å, and (h) 8 Å.

the flipper enclosure or the fields located before and after it, but it does include the guiding magnetic fields at the front and back inside the flipper enclosure.

Fig. 4(a) shows a plot of a cross-section of the magnetic field through the neutron path. Moving along the neutron path from left to right, the magnetic field gradually increases to 160 G at the entrance of the spin flipper before gradually decreases across the 24 cm long RF-field region. Fig. 4(b) shows that the simulated gradient magnetic field within the

RF-field region varies from 160 G to 40 G, with a magnetic field strength of 80 G at the center position.

An algorithm developed for tracking neutron spin procession is used to numerically solve the Bloch equations to calculate the spin change of the polarized neutrons in the magnetic field and to verify the RF-flipper's efficiency for neutrons of different wavelengths [37]. When using this method to solve the Bloch equations, it is necessary to set the parameters including neutron wavelength, magnitudes of magnetic fields in the xyz directions, step size, and direction of the neutron's initial polarization vector. The step size is defined by the spatial distance between two magnetic field vectors. When the magnetic field changes over time, the step size needs to be converted based on the neutron flight speed to ensure that the magnetic field conditions remain consistent for neutrons of different wavelengths. The change in the neutron polarization vector, adiabatic parameter, and angle between polarization vector and magnetic field can be obtained at several wavelengths with different magnetic field parameters by using this model.
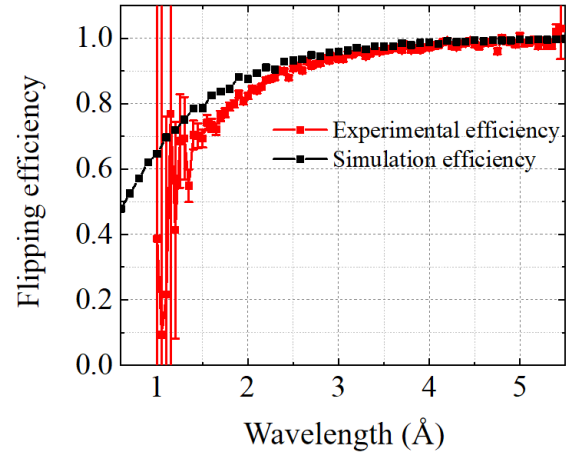

Fig. 5. The simulated and experimental flipping efficiency of the adiabatic RF-flipper for 1.0-5.5 Å polarized neutrons.

The measured gradient field $\mathbf{B}_g$ shown in Fig. 4(b) is obtained by performing Gaussmeter measurements at uniform positions along the path represented by the green line in Fig. 4(a), followed by Gaussian fitting. In the central region of the solenoid, the actual measured magnetic field is consistent with the simulated magnetic field in terms of size and trend. However, at both ends of the solenoid, there are differences between the actual and simulated magnetic fields. The actual magnetic field on the left side is about 20 G higher than the simulated one, while the actual magnetic field on the right side is about 1 G lower than the simulated one.

The amplitude of the RF-field ($\mathbf{B}_{RF}$) is measured with the detection coil at different positions inside the solenoid. When the flipper is activated, both the magnitude and frequency of the RF field remain constant, but the neutron time-of-flight through the RF-field varies directly withits wave-

length. Therefore, the longer the neutron wavelength, the more magnetic field oscillations the neutron experiences. Consequently, in the simulation, the position-dependent RF-field experienced by the neutron changes with the neutron wavelength such that $B_{\text{RF}}(l) = B_{\text{RF}} \; sin\left(\frac{B_0 \gamma_{\text{n}} l m \lambda}{h}\right)$, where $\mathbf{B}_{\text{RF}}$ as shown by the red curve in Fig. 4(c)(e)(g), m is the rest mass of a neutron, λ is the neutron wavelength, and h is Planck's constant. Expressing the RF-field as a function of position enables the simulation to be performed time-independently by simulating each neutron wavelength separately, which greatly reduces computation time.

The Bloch-equation based neutron polarization simulation is done with a 6th order Runge-Kutta method. In order to maintain accuracy through the numerical iteration process, it is necessary to decompose the magnetic field component of both the gradient magnetic field and RF-field into proper relatively infinitesimal step size, so that the magnetic field can be treated as constant in each calculation. This condition is achieved by assigning the combination of the gradient and RF-field based on the travel distance along the neutron path, so that the adiabaticity can be cross-checked based on Eq. (2). Neutrons with different wavelength are therefore treated separately with a 0.1Å step size because the difference in their travel speeds leads to different distributions of the RF-field, shown in Fig. 4(c)(e)(g). For the purpose of simplification, all simulations of the polarization transfer start with the neutron polarization vector parallel to the magnetic field outside the main RF-flipping region, so that the effect of the RF-flipping process is estimated independently. The relative phase between the RF signal and the neutron pulse are set to zero across all simulations under the condition that adiabaticity is well above 10 as defined by Eq. (2). It should be noted that while the neutron pulse and the RF signal are not synchronized, the adiabatic process within the rotating frame guarantees that the variation in phase does not cause a difference in the final polarization results. For processes that involve insufficient adiabaticity, results are averaged across all phases to simulate the actual experimental process, where signals from cumulative measurements are collected together by the neutron detector.

The simulation results of the composite magnetic field for neutrons of different wavelengths are shown in Fig. 4. In Fig. 4(c), (e), and (g), the RF-field experienced along the flight path varies depending on the neutron velocity, while the positional gradient field is identical for all neutron wavelengths. Under these simulation conditions, the changing trends of the polarization vectors in the x-direction and y-direction are similar. The polarization vector in the x-direction is not shown in Fig. 4(d), (f), and (h), allowing for a more clear observation of the changing process of the polarization vector at different positions.

As shown in Fig. 4(d), when 1 Å neutrons enter the RF-flipper, the polarization vector in the z-direction gradually decreases while the polarization vector in the y-direction gradually increases, causing the polarization vector of the neutrons to shift towards the xy-plane. After passing through the center of the RF-field, the polarization vector of the neutron undergoes a shift towards the negative z-direction, but at a noticeable angle to the z-axis. Upon exiting the RF-flipper, a significant component of the polarization vector remains within the xy-plane. This indicates that the RF flipper is not fully effective in flipping 1 Å neutrons.

For neutrons that satisfy the adiabatic condition, the action of the RF-field changes the polarization vector from the positive z-direction to the xy-plane and then to the negative z-direction, resulting in a spin-flip. The changes in the polarization vectors of 4 Å and 8 Å neutrons are as expected, and successful spin flipping has been achieved. Due to their lower velocity, the 8 Å neutrons exhibit more precession cycles during the flipping process.

The dependency of the flipping efficiency (f) on the neutron wavelength is further simulated across the wavelength range of 1.0–5.5 Å with a step size of 0.1 Å, shown as black dots in Fig. 5. It can be seen from Fig. 5 that the simulated flipping efficiency increases with the neutron wavelength. For neutrons with a wavelength of 4 Å or longer, the flipping efficiency saturates above 97%, while for neutron wavelengths shorter than 2.5 Å, the flipping efficiency is lower than 90%, which is considered insufficient. In Fig. 5, the simulated results are compared to experimental measurements to verify and illustrate the flipping process.

V.   NEUTRON EXPERIMENT RESULTS

The prototype device is constructed based on the parameters previously discussed, and its wavelength dependent flipping efficiency is tested on beamline 20 (BL-20) of the CSNS using a wavelength range of 1.0–5.5 Å selected by the neutron chopper [38–41]. The setup of the experimental components is shown in Fig. 6. A V-shaped supermirror polarizer manufactured by Swiss Neutronics with a tapered angle of 1.19° and a critical wavelength of 2 Å is used to polarize neutrons. The guide field, composed of $Nd_2Fe_{14}B$ and iron plates, maintains the polarized transmission of neutrons. Due to the internal magnetic field of the adiabatic RF-flipper being oriented oppositely to the direction of the supermirror magnetic field, a 180° rotation of the guiding magnetic field is implemented in front of the flipper to avoid a zero field region and optimized the transmission of polarized neutrons with wavelengths greater than 1 Å. The guide field generated by the wider window of the RF-flipper distributes larger stray fields then the narrower side, which can interfere with the polarized ^{3}He system and further reduce the ^{3}He analyzing ability. In order to optimize the experimental measurements and minimize interference, the narrower window of RF-flipper is arranged as the neutron incident side.

The in-house developed in-situ pumped ^{3}He neutron spin filter, utilizing adiabatic fast passage, can manipulate the polarization state of ^{3}He and serve as a neutron spin analyzer [39, 42]. With a maximum lifetime exceeding 200 hours, the system can operate stably for extended periods, and the maximum saturated ^{3}He polarization exceeds 70%, meeting experimental requirements. The detector used in the measurement is a standard ^{3}He tube detector with time-of-flight measure-
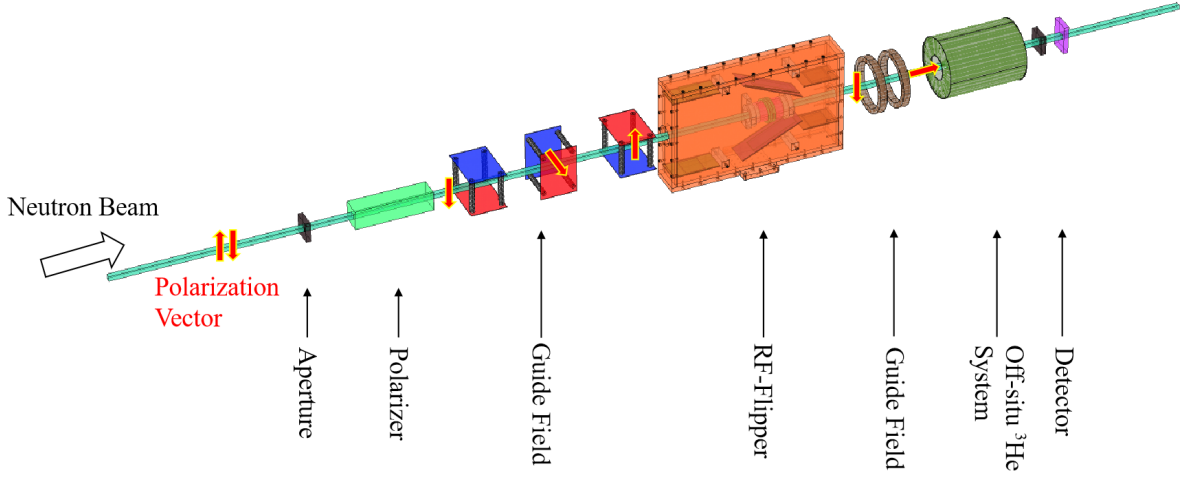
Fig. 6. Schematic diagram of the adiabatic RF-flipper experimental setup on BL-20 of the CSNS.

ment capability. The measured neutron counts are normalized to the power of the CSNS proton pulses to eliminate primary beam power fluctuations.

To obtain the flipping efficiency of the adiabatic RF-flipper, four independent neutron transmission measurements are made with a combination of the RF-flipper powered or unpowered and the ^{3}He neutron spin filter polarized parallel or anti-parallel to the magnetic field. The detection coil measured an RF-field amplitude of 22 G at the center of the solenoid when the device is switched on. The p, a, and f are the efficiencies of the supermirror polarizer, ^{3}He analyzer, and RF-flipper, respectively. In measurements $M1$ and $M2$, the RF-flipper is unpowered while the ^{3}He analyzer direction is parallel (for $M1$) and anti-parallel (for $M2$) to the magnetic guide field. Measurements $M3$ and $M4$ have the same ^{3}He analyzer state as measurements $M1$ and $M2$, respectively, except that the RF-flipper is powered. The normalized intensity of the measured values is determined by

$$M_{1,2} = \frac{1}{4}(1 \pm ap)I_0 T_a T_f T_p, \tag{3a}$$

$$M_{3,4} = \frac{1}{4}(1 \pm afp)I_0 T_a T_f T_p. \tag{3b}$$

where I_0 is the neutron beam intensity normalized to the proton beam power and T_a, T_f, and T_p are the proportion of neutron transmission through the analyzer, RF-flipper, and polarizer, respectively. From these quantities, it follows that

$$f = \left(\frac{M_4 - M_3}{M_4 + M_3}\right) \Big/ \left(\frac{M_1 - M_2}{M_1 + M_2}\right) \tag{4}$$

The measured flipping efficiency, shown as red dots in Fig. 5, exceeds 97% for polarized neutrons with a wavelength greater than 4Å. It can be seen that as the neutron wavelength increases, both the simulated and experimental flipping efficiency increase. The experimental efficiency of the RF-flipper is lower than the simulation results across all wavelengths. The divergence is discovered to be caused by the per-

manent magnets of the RF-flipper not being installed symmetrically, leading to a significant magnetic field gradient at the beam interface and thereby reducing the flipping efficiency. Furthermore, the simulated flipping efficiency is based on the centerline of the RF-flipper, while the experimental results include data from the entire neutron beam cross-section transmitted through the RF-flipper, which leads to discrepancies of the flipping efficiency results in the short wavelength range.

The difference between the simulation and experiment is further examined by analyzing the irregular gradient field in the effective beam cross-section depicted in Fig. 7(a). A clear variation from the central field of 80 G is observed, ranging from 88 G at the top of the effective neutron beam region to 80 G at the center of the solenoid, and ranging from 72.5 G at the far left of the effective neutron beam region to 80 G at the center of the solenoid. Thus, in the experiment as the neutron beam traverses regions away from the center of the solenoid, the non-uniform gradient field leads to a reduction in the flipping efficiency.

The discrepancy is estimated by averaging the polarization transfer across eight locations, 2.5 cm from center in the beam region, and the results are shown in Fig. 7(b). The green and black simulated results utilize the wavelength-dependent RF-field profiles plotted in Fig. 4(c)(e)(g), and the position-dependent gradient field plotted in Fig. 7(a). In comparison to the centerline simulation results which overestimated the flipping efficiency, the off-center simulation results are much lower than the experimental results. This result shows that the entire gradient field region traversed by the neutron beam must be considered to create a more accurate simulation. Multiple averages and calculations are done for the total cross section to compare to the experimental results. It has been observed that the magnetic field configuration can be easily influenced by the surrounding environment, which leads to variations in the final flipping efficiency.

The simulation results also provide the adiabatic parameters of polarized neutrons at different positions: $\kappa = \frac{B\gamma_n}{\frac{d\theta}{dl}} \cdot \frac{m\lambda}{h}$,
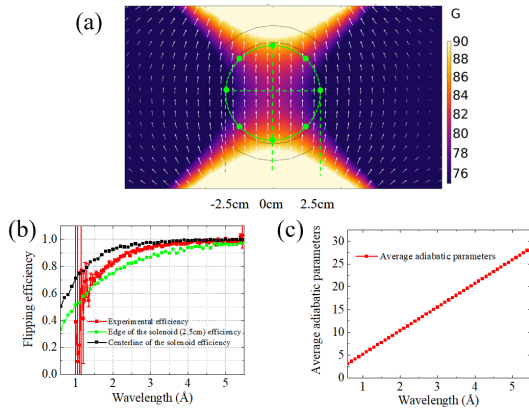
Fig. 7. (a) Cross-sectional view at the center of the solenoid. The white arrows are the directions of the magnetic field lines. The eight green dots are symmetrically distributed on a circle with a radius of 2.5 cm from the center of the solenoid. (b) The green points are the simulated average flipping efficiency of neutrons traversing through the locations of the green dots in (a). The black and red points are the simulated flipping efficiency along the centerline of the solenoid and the experimental flipping efficiency, respectively, as previously shown in Fig. 5. (c) Average adiabatic parameter of different wavelengths.

where κ represents the adiabatic parameter, θ is the angle of the adjacent magnetic field variations vector, l is the distance the neutron travels and B is the magnetic field strength. After transforming the magnetic field in Fig. 4 from the laboratory frame to the rotating frame, the average adiabatic parameter for neutrons ranging from 0.6 Å to 5.5 Å varies with wavelength, as shown in Fig. 7(c). It is observed that as the wavelength increases, the average adiabatic parameter of polarized neutrons exhibits a linear upward trend, which aligns with the theoretical principles. However, even with an average adiabatic parameter of 10 for 2 Å neutrons, which meets the adiabatic condition, simulation results indicate a flipping efficiency of only 90% for these neutrons. The investigation implies that phase difference in the simulation does not cause the dropping of the flipping efficiency, and the numerical simulation remains valid for the purpose of understanding the flipping process.

VI. CONCLUSION AND DISCUSSION

We have successfully designed and manufactured an adiabatic RF-flipper prototype at the China Spallation Neutron Source based on the principles of RF-flipper operation, and the parameters have been optimized for our application. By analyzing the neutron wavelength and flipping efficiency dependence with simulations and computer-aided design techniques, precise designs of adiabatic RF-flippers for specific environments can be achieved. The prototype is tested at BL-20 over a wavelength range of 0.6 Å to 5.5 Å, and a flipping efficiency of 97% is achieved for neutrons with wavelength above 4 Å. The discrepancy between the design simulations and experiment is caused by an irregular gradient field, and its effect has been investigated through follow-up simulations.

For future applications, an adiabatic RF-flipper device can now be designed in-house while satisfying various beamline conditions. Future designs can be improved by optimizing the gradient field design to be more uniform throughout the entire transverse cross-section of the neutron beam path through the RF-field region and improving the RLC-circuit to allow for a stronger power output.

[1] S. V. Maleev, Polarized neutron scattering in magnets. Phys. Usp. **45**, 569 (2002). https://doi.org/10.1070/PU2002V045N06ABEH001017
[2] A. Wiedenmann, Small-angle neutron scattering investigations of magnetic nanostructures and interfaces using polarized neutrons. Physica B **297**, 1-4 (2001). https://doi.org/10.1016/S0921-4526(00)00872-3
[3] S. Koizumi, H. Iwase, J. Suzuki et al., Focusing and polarized neutron small-angle scattering spectrometer (SANS-J-II). The challenge of observation over length scales from ångström to a micrometer. J. Appl. Crystallogr. **40**, s474-s479 (2007). https://doi.org/10.1107/S0021889807014392
[4] G. P. Felcher, R. O. Hilleke, R. K. Crawford et al., Polarized neutron reflectometer a new instrument to measure magnetic depth profiles. Rev. Sci. Instrum. **58**, 609-619 (1987). https://doi.org/10.1063/1.1139225
[5] J. F. Ankner and G. P. Felcher, Polarized neutron reflectometry. J. Magn. Magn. Mater. **200**, 1-3 (1999). https://doi.org/10.1016/S0304-8853(99)00392-3
[6] M. Strobl, N. Kardjilov, A. Hilger et al., Imaging with polarized neutrons. Physica B **404**, 2611-2614 (2009). https://doi.org/10.1016/j.physb.2009.06.032
[7] N. Kardjilov, I. Manke, A. Hilger et al., Neutron imaging in materials science. Mater. Today. **14**, 248-256 (2011). https://doi.org/10.1016/S1369-7021(11)70139-0
[8] A. Zheludev, V. Barone, M. Bonnet et al., Spin density in a nitronyl Nitroxide Free Radical. Polarized neutron diffraction investigation and ab initio calculations. J. Am. Chem. Soc. **116**, 2019-2027 (1994). https://doi.org/10.1021/ja00084a048
[9] J. Akimitsu, H. Ichikawa, N. Eguchi et al., Direct observation of orbital ordering in YTiO3 by means of the polarized neutron diffraction technique. J. Phys. Soc. Jpn. **70**, 3475-3478 (2001). https://doi.org/10.1143/jpsj.70.3475
[10] F. Mezei, Neutron Spin Echo: A New Concept in Polarized Thermal Neutron Techniques. Z. Physik **255**, 146-160 (1972). https://doi.org/10.1007/BF01394523
[11] R. Golub and R. Gähler, A neutron resonance spin echo spectrometer for quasi-elastic and inelastic scattering. Phys. Lett. A **123**, 43-48 (1987). https://doi.org/10.1016/0375-9601(87)90760-2
[12] A. Salman, J. Zhou, J. Yang, et al., Development of Time-of-Flight Polarized Neutron Imaging at the China Spallation Neutron Source. Chin. Phys. Lett. **39**, 062901 (2022). https://doi.org/10.1088/0256-307X/39/6/062901

[13] D. Honecker, A. Ferdinand, F. Döbrich, et al., Longitudinal polarization analysis in small-angle neutron scattering. Eur. Phys. J. B **76**, 209-213 (2010). https://doi.org/10.1140/epjb/e2010-00191-5

[14] O. Schärpf and H. Capellmann, The XYZ-Difference Method with Polarized Neutrons and the Separation of Coherent, Spin Incoherent, and Magnetic Scattering Cross Sections in a Multidetector. Phys. Status Solidi A-Appl. Mat. **135**, (1993). https://doi.org/10.1002/pssa.2211350204

[15] J. R. Stewart, P. P. Deen, K. H. Andersen et al., Disordered materials studied using neutron polarization analysis on the multi-detector spectrometer, D7. J. Appl. Crystallogr. **42**, 69-84 (2009). https://doi.org/10.1107/S0021889808039162

[16] F. Tasset, Zero field neutron polarimetry. Physica B **156**, 627-630 (1989). https://doi.org/10.1016/0921-4526(89)90749-7

[17] F. Tasset, P. J. Brown and J. B. Forsyth, Determination of the absolute magnetic moment direction in Cr2O3 using generalized polarization analysis. J. Appl. Phys. **63**, 3606-3608 (1988). https://doi.org/10.1063/1.340709

[18] P. J. Brown, J. B. Forsyth and F. Tasset, Neutron polarimetry. Proc. R. Soc. Lond. A **442**, 147-160 (2007). https://doi.org/10.1098/rspa.1993.0096

[19] J. B. Ajo-Franklin, S. Dou, N. J. Lindsey et al., Distributed Acoustic Sensing Using Dark Fiber for Near-Surface Characterization and Broadband Seismic Event Detection. Sci Rep 9, 1328 (2019). **9**, 147-160 (2007). https://doi.org/10.1038/s41598-018-36675-8

[20] T. Wang, S. R. Parnell, W. A. Hamilton et al., Compact spherical neutron polarimeter using high-T(c) YBCO films. Rev Sci Instrum. **87**, 033901 (2016). https://doi.org/10.1063/1.4943254

[21] R. Maruyama, T. Ebisawa, S. Tasaki et al., A resonance neutron-spin flipper for neutron spin echo at pulsed sources. Physica B **335**, 238-242 (2003). https://doi.org/10.1016/S0921-4526(03)00246-1

[22] A. N. Bazhenov, V. M. Lobashev, A. N. Pirozhkov et al., An adiabatic resonance spin-flipper for thermal and cold neutrons. Nucl. Instrum. Methods Phys. Res. Sect. A-Accel. Spectrom. Dect. Assoc. Equip. **332**, 534-536 (1993). https://doi.org/10.1016/0168-9002(93)90311-5

[23] Chen W C, Erwin R, Tsai P, et al., A large beam high efficiency radio frequency neutron spin flipper. Rev. Sci. Instrum. **92**, (2021). https://doi.org/10.1063/5.0045687

[24] T. J. L. Jones and W. G. Williams, Non-adiabatic spin flippers for thermal neutrons. Nucl. Instrum. Methods **152**, 463-469 (1978). https://doi.org/10.1016/0029-554X(78)90047-2

[25] R. Pynn, Broadband spin flippers constructed from thin magnetic films. Physica B **40**, s474-s479 (2007). https://doi.org/10.1107/S0021889807014392

[26] P.-N. Seo, L. Barro´n-Palos, J. D. Bowman et al., High-efficiency resonant rf spin rotator with broad phase space acceptance for pulsed polarized cold neutron beams. Phys. Rev. ST Accel. Beams **11**, 084701 (2008). https://doi.org/10.1103/PhysRevSTAB.11.084701

[27] M. R. Fitzsimmons, M. Lütt, H. Kinder et al., YBCO films as Meissner screens in the control of polarized neutron beams — Observations and calculations. Nucl. Instrum. Meth. A. **411**, 401-416 (1998). https://doi.org/10.1016/S0168-9002(98)00008-4

[28] Y. C. Dong, T. H. Wang, W. Kreuzpaintner et al., Miniaturized time-of-flight neutron spin flipper using a high-Tc superconductor. Nucl. Sci. Tech. **33**, 145 (2022). https://doi.org/10.1007/s41365-022-01134-7

[29] S. R. Parnell, A. L. Washington, H. Kaiser et al., Performance of a polarised neutron cryo-flipper using a high TcYBCO film. Nucl. Instrum. Meth. A **722**, 20-23 (2013). https://doi.org/10.1016/J.NIMA.2013.04.041

[30] V. T. Lebedev and G. Török, Broadband neutron spin-flippers on magnetized foils. Nucl. Instrum. Meth. B. **195**, 449-454 (2002). https://doi.org/10.1016/S0168-583X(02)01144-8

[31] S. V. Grigoriev, A. I. Okorokov and V. V. Runov, Peculiarities of the construction and application of a broadband adiabatic flipper of cold neutrons. Nucl. Instrum. Meth. A **384**, 451-456 (1997). https://doi.org/10.1107/S0021889807014392

[32] H. Chen and X. L. Wang, China's first pulsed neutron source. Nature Mater. **15**, 689-691 (2016). DOI: 10.1038/nmat4655

[33] J. Wei, S. N. Fu, J. Y. Tang et al., China Spallation Neutron Source - an overview of application prospects Chin. Phys. C **33**, 1033 (2009). https://doi.org/10.1038/nmat4655

[34] J. Y. Tang, Q. An, J. B. Bai et al., Back-n white neutron source at CSNS and its applications. Nucl. Sci. Tech. **32**, 11 (2021). https://doi.org/10.1007/s41365-021-00846-6

[35] R. T. Robiscoe, A Spin Flip Problem. Am. J. Phys. **39**, 146-150 (1971). https://doi.org/10.1119/1.1986080

[36] COMSOL AB, COMSOL Multiphysics ® v.6.0. cn.comsol.com Stockholm, Sweden.

[37] P. A. Seeger and L. L. Daemen, Numerical solution of Bloch's equation for neutron spin precession. **457**, 338-346 (2001). https://doi.org/10.1016/S0168-9002(00)00769-5

[38] L. Tian, A. Salman, C. Y. Huang et al., Developing time-of-flight polarized neutron capability at the China Spallation Neutron Source. Nucl. Sci. Tech. **34**, 146 (2023). https://doi.org/10.1007/s41365-023-01286-0

[39] J. P. Zhang, C. Y. Huang, Z. C. Qin et al., In-situ optical pumping for polarizing 3He neutron spin filters at the China Spallation Neutron Source. Sci. China. Phys. Mech. **65**, 241011 (2022). https://doi.org/10.1007/s11433-021-1876-0

[40] Z. C. Qin, C. Y. Huang, Z. N. Buck et al., Development of a 3He Gas Filling Station at the China Spallation Neutron Source. Chin. Phys. Lett. **38**, 052801 (2021). https://doi.org/10.1088/0256-307X/38/5/052801

[41] C. Y. Huang, J. P. Zhang, F. Ye et al., Development of a Spin-Exchange Optical Pumping-Based Polarized 3He System at the China Spallation Neutron Source (CSNS). Chin. Phys. Lett. **38**, 092801 (2021). https://doi.org/10.1088/0256-307X/38/9/092801

[42] X. Tong, C. Y. Jiang, V. Lauter et al., In situ polarized 3He system for the Magnetism Reflectometer at the Spallation Neutron Source. Rev. Sci. Instrum. **83**, (2012). https://10.1063/1.4731261